
Reciprocal Adversarial Learning via Characteristic Functions

Shengxi Li

Department of Electrical and Electronic Engineering
Imperial College London
shengxi.li17@imperial.ac.uk

Zeyang Yu

Department of Electrical and Electronic Engineering
Imperial College London
z.yu17@imperial.ac.uk

Min Xiang

Department of Electrical and Electronic Engineering
Imperial College London
m.xiang13@imperial.ac.uk

Danilo Mandic

Department of Electrical and Electronic Engineering
Imperial College London
d.mandic@imperial.ac.uk

Abstract

Generative adversarial nets (GANs) have become a preferred tool for accommodating complicated distributions, and to stabilise the training and reduce the mode collapse of GANs, one of their main variants employs the integral probability metric (IPM) as the loss function. Although theoretically supported, extensive IPM-GANs are basically comparing moments in an embedded domain of the *critic*. We generalise this by comparing the distributions rather than the moments via a powerful tool, i.e., the characteristic function (CF), which uniquely and universally contains all the information about a distribution. For rigour, we first establish the physical meaning of the phase and amplitude in CFs. This provides a feasible way of manipulating the generation. We then develop an efficient sampling way to calculate the CFs. Within this framework, we further prove an equivalence between the embedded and data domains when a reciprocal exists, which allows us to develop the GAN in an auto-encoder way, by using only two modules to achieve bi-directionally generating clear images. We refer to this efficient structure as the reciprocal CF GAN (RCF-GAN). Experimental results show the superior performances of the proposed RCF-GAN in terms of both generation and reconstruction.

1 Introduction

Generative adversarial nets (GANs) have achieved impressive success by virtue of its powerful capability in capturing complicated data distributions [1]. In practical applications, however, their significant potential still remains under-explored as GANs typically suffer from unstable training and mode collapse issues [2]. An effective yet elegant way to address these issues is to replace the

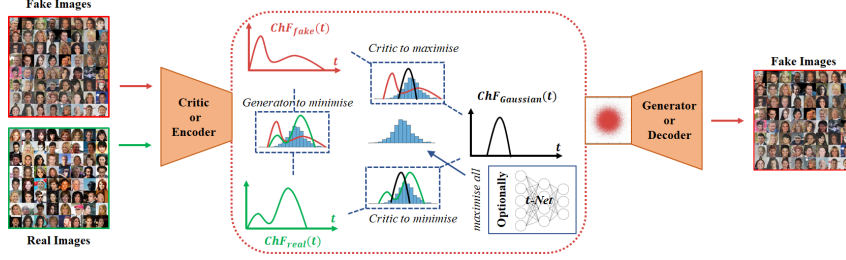


Figure 1: The overall structure of the proposed RCF-GAN. The generator serves to minimise the CF loss between the embedded real and fake distributions. The *critic* serves to minimise the CF loss between the embedded real and the input noise distributions, whilst maximising the CF loss between the embedded fake and the input noise distributions. Moreover, an MSE loss between the embedded fake and the input noise distributions is regularised as the auto-encoder loss, which has not been shown in the figure. An optional *t*-net can be employed to optimally sample the CF loss.

Jensen-Shannon (JS) divergence in measuring the discrepancy in the original form of GANs [3] by another class of metrics called the integral probability metric (IPM) [4] given by,

$$d(\mathcal{P}_d, \mathcal{P}_g) = \sup_{f \in \mathcal{F}} |\mathbb{E}_{x \sim \mathcal{P}_d}[f(x)] - \mathbb{E}_{x \sim \mathcal{P}_g}[f(x)]|, \quad (1)$$

where the symbol \mathcal{F} in IPMs represents a collection of (typically real) bounded functions, \mathcal{P}_g denotes the generated distribution, and \mathcal{P}_d is the real data distribution. Using IPMs to improve GANs has been justified by the fact that in real-world data distributions are typically embedded in low-dimensional manifolds, which is intuitive because data preserve semantic information instead of being a collection of rather random pixels. Thus, the divergence measure (“bin-to-bin” comparison) of the original GAN could easily max out, whereas the IPMs such as the Wasserstein distance (“cross-bin” comparison) can consistently yield a meaningful measure between the generated and real data distributions [3].

Varying collections of \mathcal{F} in (1), therefore, define different IPM-GANs and the supremum $\sup_{f \in \mathcal{F}}$ is then typically achieved by the discriminator net, or more formally, the *critic* in the IPM-GANs. The first IPM-GAN was motivated by the Wasserstein GAN (W-GAN) [5], where \mathcal{F} denotes all the 1-Lipschitz functions. However, it has been widely argued that the *critic* is not powerful enough to search within all the 1-Lipschitz function spaces, which leads to limited diversity of the generator due to an ill-posed equivalence measurement of \mathcal{P}_d and \mathcal{P}_g [6, 7]. Follow-up works have been proposed to improve the W-GAN by either enhancing it to satisfy the 1-Lipschitz condition (e.g., by gradient penalty [8] or spectral normalization [9]) or by employing *easy-to-implement* \mathcal{F} for the *critic*. The latter, by virtue of relaxing the *critic*, typically leads to a stringent comparison on the embedded feature domain, i.e., by matching higher-order moments instead of the mean matching in the W-GAN. This path includes many recent GANs of additionally considering the second-order moment (e.g., Fisher-GAN [10] and McGAN [11]), together with explicitly (e.g., Sphere GAN [12]) or implicitly (e.g., MMD-GAN [13, 14]) comparing higher-order moments. We refer to the *Related Works* section in the supplementary material for a detailed analysis on different IPM-GANs.

Generalising (1) as moment matching has been justified as a natural and beneficial way when understanding IPM-GANs [15–17]. This also compensates for the deficiency where the *critic* may not transform the data distributions into unimodal distributions, for example, the Gaussian distribution that is solely determined by the first- and second-order moments. Moreover, it is even more safe to compare the distributions because the equivalence in distributions ensures the equivalence in moments; the inverse, however, does not necessarily hold. As a powerful tool of containing all the information relevant to a distribution, the *characteristic function* (CF) provides a universal way of comparing distributions even when their probability density functions (pdfs) do not exist. The CF also has a one-to-one correspondence to the cumulative density function (cdf), which has also been verified to benefit the design of GANs [18]. Compared to the moment generating function (mgf) that has been reflected in the MMD-GAN [13], the CF is unique and universally existent. More importantly, the CF is automatically aligned at 0; this means that even a simple “bin-to-bin” comparison between CFs can consistently provide a meaningful measure and thus avoid gradient vanishing that appears in the original GAN [5]. On the other hand, the weak convergence property of CFs ensures that the convergence in the CF also indicates the convergence in the distributions.

In this paper, we propose a reciprocal CF GAN (RCF-GAN) as a natural generalisation of the existing IPM-GANs, with the overall structure shown in Fig. 1. It needs to be pointed out that incorporating the CF in a GAN is non-trivial because the CF is basically complex-valued and the comparison has to be performed on functions as well. To address these difficulties, we first demystify the role of CFs by finding that its phase is closely related to the distribution centre, whereas the amplitude dominates the distribution scale. This provides a feasible way of balancing the accuracy and diversity of generation. Then, as for the comparison over functions, we prove that other than in the whole space of CFs, sampling within a small ball around 0 of CFs is sufficient to compare two distributions. We further optimise the sampling strategy by automatically adjusting sampling distributions under the umbrella of the *scale mixture of normals* [19]. Moreover, because we are comparing in the embedded feature domain, we prove its equivalence to the counterpart in the data domain when a reciprocal between the generator and the *critic* holds. This motivates us to incorporate an auto-encoder structure to satisfy this theoretical requirement. Different from many existing adversarial works with auto-encoders incorporating at least three modules¹ [13, 14, 21–26], our RCF-GAN only requires two modules that already exist in a GAN; the *critic* is an encoder and the generator is a decoder as well, which is neat and reasonable as this comes without increasing computational complexity and without other requirements such as the Lipschitz continuity. More importantly, by only comparing distributions in the embedded domain, our CF-GAN avoids the smoothing artefact that arises from the use of point-wise mean square error (MSE) employed in the data domain, and thus benefits from both the auto-encoder and the GANs, i.e., *bi-directionally* generating *clear* images. Our experimental results show that by employing a naive structure, our RCF-GAN achieves remarkable improvements on the generation, together with an additional gain in the reconstruction. The performance of our RCF-GAN² can be further improved by many orthogonal techniques, e.g., progressively training [28], using individual learning rates [29], spectral normalisation [9] or adding noise to discriminators [3].

2 Characteristic Function Loss and Efficient Sampling Strategy

2.1 Characteristic Function and Elliptical Distribution

The CF of a random variable $\mathcal{X} \in \mathbb{R}^m$ represents the expectation of its complex unitary transform, given by

$$\Phi_{\mathcal{X}}(\mathbf{t}) = \mathbb{E}_{\mathcal{X}}[e^{j\mathbf{t}^T \mathbf{x}}] = \int_{\mathbf{x}} e^{j\mathbf{t}^T \mathbf{x}} dF_{\mathcal{X}}(\mathbf{x}), \quad (2)$$

where $F_{\mathcal{X}}(x)$ is the cdf of \mathcal{X} . We thus have $\Phi_{\mathcal{X}}(\mathbf{0}) = 1$ and $|\Phi_{\mathcal{X}}(\mathbf{t})| \leq 1$ for all \mathbf{t} . This property ensures that CFs can be straightforwardly compared in a “bin-to-bin” manner, because all CFs are automatically aligned at $\mathbf{t} = \mathbf{0}$. Moreover, when the pdf of \mathcal{X} exists, the expression in (2) is equal to its inverse Fourier transform; this ensures that $\Phi_{\mathcal{X}}(\mathbf{t})$ is uniformly continuous. Another important property of the CF is that it uniquely and universally retains all the information of a random variable. In other words, a random variable does not necessarily need to possess a pdf (e.g., when it is an α -stable distribution), but its CF always exists.

As the cdf $F_{\mathcal{X}}(\mathbf{x})$ is unknown and is to be compared, we employ the empirical characteristic function (ECF) as an asymptotic approximation in the form of $\hat{\Phi}_{\mathcal{X}_n}(\mathbf{t}) = \sum_{i=1}^n e^{j\mathbf{t}^T \mathbf{x}_i}$, where $\{\mathbf{x}_i\}_{i=1}^n$ are n i.i.d samples drawn from \mathcal{X} . As a result of the *Levy continuity theorem* [30], the ECF converges weakly to the population CF [31]. More importantly, the *uniqueness theorem* guarantees that two random variables have the same distribution if and only if their CFs are identical [32]. Therefore, together with the weak convergence, the ECF provides a feasible and good proxy to the distribution, which has also been preliminarily applied in two sample test [33, 34]. Before proceeding further, we introduce an important class of distributions that will be mentioned later.

Example 1. *In unimodal distributions, there is one broad class of distributions called the elliptical distribution, which is general enough to include various typical distributions such as the Gaussian, Laplace, Cauchy, Student-t, α -stable and logistic distributions. The elliptical distributions do not*

¹To our best knowledge, the only exception is the AGE [20], which adopts two modules in an auto-encoder under a max-min problem and different losses. Please see the *Related Works* for the details.

²We notice a very recent independent work [27] which also employs the CF as a replacement by using the same structure of MMD-GANs. Our RCF-GAN, however, is substantially different from that in [27] in terms of the analysis on decomposing CFs, CF losses, theoretical guarantees, GAN structures, etc. Our achieved results are also superior to those in [27], where all images were evaluated under the size of 32×32 .

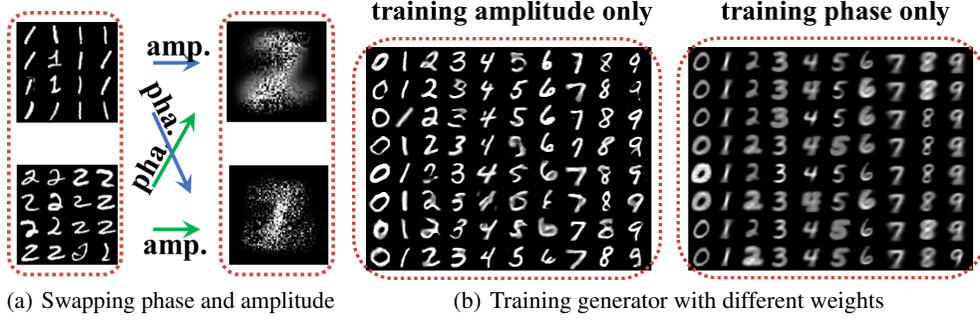


Figure 2: Two illustrations on the MNIST dataset which show the physical meaning of the phase and amplitude of the CF. (a) We fit a multivariate Gaussian for the images of digits 1 and 2, by naively assuming that each pixel is independent from other pixels. Then, we swap the phase and amplitude information of the CFs between the two multivariate distributions, and then randomly sample from the swapped distributions. (b) We directly train a generator given the images of each digit. To avoid the impact from the *critic*, we *do not* employ the *critic* in this experiment and directly calculate the loss between images after the generator with different α . We train amplitude only for $\alpha = 1$ and phase only for $\alpha = 0$.

necessarily have pdfs and we refer to [35] for more detail. The CF of an elliptical distribution, \mathcal{X} , however, always exists and has the following form

$$\Phi_{\mathcal{X}}(\mathbf{t}) = e^{j\mathbf{t}^T \boldsymbol{\mu}} \psi(\mathbf{t}^T \boldsymbol{\Sigma} \mathbf{t}), \quad (3)$$

where $\boldsymbol{\mu}$ denotes the distribution centre and $\boldsymbol{\Sigma}$ is the distribution scale, and $\psi(\cdot)$ is a real-valued scalar function, for example, $\psi(s) = e^{(-s/2)}$ for the Gaussian distribution. By inspecting (3) we can easily find that the phase of the CF is solely related to the location of data centre and the amplitude is only governed by the distribution scale (diversity).

2.2 Distance Measure via Characteristic Functions

The auto alignment property of the CFs allows us to incorporate a simple “bin-to-bin” comparison over two complex-valued CFs (corresponding to two random variables \mathcal{X} and \mathcal{Y}), in the form

$$\mathcal{C}_{\mathcal{T}}(\mathcal{X}, \mathcal{Y}) = \int_{\mathbf{t}} \underbrace{((\Phi_{\mathcal{X}}(\mathbf{t}) - \Phi_{\mathcal{Y}}(\mathbf{t}))(\Phi_{\mathcal{X}}^*(\mathbf{t}) - \Phi_{\mathcal{Y}}^*(\mathbf{t})))}_{c(\mathbf{t})}^{1/2} dF_{\mathcal{T}}(\mathbf{t}), \quad (4)$$

where Φ^* denotes the complex conjugate of Φ and $F_{\mathcal{T}}(\mathbf{t})$ is the cdf of a sampling distribution on \mathbf{t} . For the convenience of subsequent analysis, we represent the quadratic term for each \mathbf{t} as $c(\mathbf{t}) = (\Phi_{\mathcal{X}}(\mathbf{t}) - \Phi_{\mathcal{Y}}(\mathbf{t}))(\Phi_{\mathcal{X}}^*(\mathbf{t}) - \Phi_{\mathcal{Y}}^*(\mathbf{t}))$. More importantly, $\mathcal{C}_{\mathcal{T}}(\mathcal{X}, \mathcal{Y})$ is a valid distance that measures the difference of two random variables via CFs, of which the proof is provided in Lemma 1; this means $\mathcal{C}_{\mathcal{T}}(\mathcal{X}, \mathcal{Y}) = 0$ if and only if $\mathcal{X} =^d \mathcal{Y}$. A specific type of $\mathcal{C}_{\mathcal{T}}(\mathcal{X}, \mathcal{Y})$ in (4) is when the pdf of \mathbf{t} is proportional to $\|\mathbf{t}\|^{-1}$, and its relationship to other metrics, including the Wasserstein and Kolmogorov distances, has been analysed in detail [36]. Please note that in this paper, we move all the proofs to the supplementary material.

Lemma 1. *The discrepancy between \mathcal{X} and \mathcal{Y} , given by $\mathcal{C}_{\mathcal{T}}(\mathcal{X}, \mathcal{Y})$ in (4), is a distance metric when the support of \mathcal{T} resides in \mathbb{R}^m .*

Furthermore, as the phase and amplitude of a CF indicate the data centre and diversity, we inspect $c(\mathbf{t})$ and rewrite it in a physically meaningful way, i.e., through the differences in the corresponding phase and amplitude terms as [37],

$$\begin{aligned} c(\mathbf{t}) &= |\Phi_{\mathcal{X}}(\mathbf{t})|^2 + |\Phi_{\mathcal{Y}}(\mathbf{t})|^2 - \Phi_{\mathcal{X}}(\mathbf{t})\Phi_{\mathcal{Y}}^*(\mathbf{t}) - \Phi_{\mathcal{Y}}(\mathbf{t})\Phi_{\mathcal{X}}^*(\mathbf{t}) \\ &= |\Phi_{\mathcal{X}}(\mathbf{t})|^2 + |\Phi_{\mathcal{Y}}(\mathbf{t})|^2 - |\Phi_{\mathcal{X}}(\mathbf{t})||\Phi_{\mathcal{Y}}(\mathbf{t})|(2 \cos(\mathbf{a}_{\mathcal{X}}(\mathbf{t}) - \mathbf{a}_{\mathcal{Y}}(\mathbf{t}))) \\ &= |\Phi_{\mathcal{X}}(\mathbf{t})|^2 + |\Phi_{\mathcal{Y}}(\mathbf{t})|^2 - 2|\Phi_{\mathcal{X}}(\mathbf{t})||\Phi_{\mathcal{Y}}(\mathbf{t})| + 2|\Phi_{\mathcal{X}}(\mathbf{t})||\Phi_{\mathcal{Y}}(\mathbf{t})|(1 - \cos(\mathbf{a}_{\mathcal{X}}(\mathbf{t}) - \mathbf{a}_{\mathcal{Y}}(\mathbf{t}))) \\ &= \underbrace{(|\Phi_{\mathcal{X}}(\mathbf{t})| - |\Phi_{\mathcal{Y}}(\mathbf{t})|)^2}_{\text{amplitude difference}} + 2|\Phi_{\mathcal{X}}(\mathbf{t})||\Phi_{\mathcal{Y}}(\mathbf{t})| \underbrace{(1 - \cos(\mathbf{a}_{\mathcal{X}}(\mathbf{t}) - \mathbf{a}_{\mathcal{Y}}(\mathbf{t})))}_{\text{phase difference}}, \end{aligned} \quad (5)$$

where $\mathbf{a}_{\mathcal{X}}(\mathbf{t})$ and $\mathbf{a}_{\mathcal{Y}}(\mathbf{t})$ represent the angles of $\Phi_{\mathcal{X}}(\mathbf{t})$ and $\Phi_{\mathcal{Y}}(\mathbf{t})$, respectively. Therefore, we can clearly see that $\mathcal{C}_{\mathcal{T}}(\mathcal{X}, \mathcal{Y})$ basically measures the amplitude difference and the phase difference weighted by the amplitudes. We can further add a convex combination of the two terms via $0 \leq \alpha \leq 1$:

$$c_{\alpha}(\mathbf{t}) = \alpha(|\Phi_{\mathcal{X}}(\mathbf{t})| - |\Phi_{\mathcal{Y}}(\mathbf{t})|)^2 + (1 - \alpha)(2|\Phi_{\mathcal{X}}(\mathbf{t})||\Phi_{\mathcal{Y}}(\mathbf{t})|(1 - \cos(\mathbf{a}_{\mathcal{X}}(\mathbf{t}) - \mathbf{a}_{\mathcal{Y}}(\mathbf{t}))). \quad (6)$$

Recall that for the elliptical distributions in Example 1, the phase represents the distribution centre while the amplitude represents the scale; $\mathcal{C}_{\mathcal{T}}(\mathcal{X}, \mathcal{Y})$ thus measures the both discrepancy of the centres and diversity of two distributions. We show in Figure 2-(a) that by swapping the phase and amplitude parts, the saliency information follows the phase part of the CF, which captures the centres of the distribution. We further illustrate in Figure 2-(b) that this property still holds in real data distributions, even though they are much complicated and even non-unimodal. From Figure 2-(b), solely training the phase results to generating images similar to an average of the real data, as a result of minimising the difference on the data centres. On the other hand, when training the amplitude only, we can obtain diversified but inaccurate images (some digits are wrongly generated). Therefore, by using different weights in $c_{\alpha}(\mathbf{t})$, we can flexibly capture the main content via minimising the phase difference, whilst enriching the diversity of generated images by increasing the amplitude loss. This provides a meaningful and feasible way of understanding the GAN loss in controlling the generation.

The term $\int_{\mathbf{t}} c(\mathbf{t}) dF_{\mathcal{T}}(\mathbf{t})$ contained in our CF loss can also be employed to optimise the form of kernels via optimising $F_{\mathcal{T}}(\mathbf{t})$, whereas the kernels are fixed in the MMD-GANs. This is due to the fact that the shift invariant and characteristic kernels in the MMD metric have to satisfy $k(\mathbf{x}, \mathbf{y}) = \int_{\mathbf{t}} e^{-j\mathbf{t}^T(\mathbf{x}-\mathbf{y})} dF_{\mathcal{T}}(\mathbf{t})$ for some compactly supported $F_{\mathcal{T}}(\mathbf{t})$ [38]. Thus, the elliptical distributions in Example 1 potentially provide a set of well-defined characteristic kernels, by choosing $F_{\mathcal{T}}(\mathbf{t})$ as a normalised version of the CFs in (3). Then, the corresponding real-valued kernels are the density generators in [19]. We introduce in the next section a way of optimising $F_{\mathcal{T}}(\mathbf{t})$.

2.3 Sampling the Characteristic Function Loss

In practice, to calculate $\mathcal{C}_{\mathcal{T}}(\mathcal{X}, \mathcal{Y})$ efficiently, as mentioned in Section 2.1, $\Phi_{\mathcal{X}}(\mathbf{t})$ and $\Phi_{\mathcal{Y}}(\mathbf{t})$ can be evaluated by the ECFs of \mathcal{X} and \mathcal{Y} , which are weakly convergent to the corresponding population CFs. The remaining task is to sample from $F_{\mathcal{T}}(\mathbf{t})$. A direct approach is to use the neural net where the input is Gaussian noise and the output is the samples of $F_{\mathcal{T}}(\mathbf{t})$. However, Proposition 1 indicates that this can lead to ill-posed optima whereby $F_{\mathcal{T}}(\mathbf{t})$ converges to some point mass distributions. In our experiment, we also found that directly optimising $F_{\mathcal{T}}(\mathbf{t})$ can cause instability.

Proposition 1. *The maximum of $\mathcal{C}_{\mathcal{T}}(\mathcal{X}, \mathcal{Y})$ is reached when $F_{\mathcal{T}}(\mathbf{t})$ attains a mass point at \mathbf{t}^* , where $\mathbf{t}^* = \arg \max_{\mathbf{t}} c(\mathbf{t})$. The minimum of $\mathcal{C}_{\mathcal{T}}(\mathcal{X}, \mathcal{Y})$ is reached when $F_{\mathcal{T}}(\mathbf{t})$ attains a mass point at $\mathbf{0}$.*

In the way of addressing this ill-posed optimisation on $F_{\mathcal{T}}(\mathbf{t})$, we can impose some constraints on $F_{\mathcal{T}}(\mathbf{t})$, for example, by assuming some parametric distributions. On the other hand, we may also be concerned that the constraints on $F_{\mathcal{T}}(\mathbf{t})$ can impede the ability of $\mathcal{C}_{\mathcal{T}}(\mathcal{X}, \mathcal{Y})$ as a metric to distinguish \mathcal{X} from \mathcal{Y} . Lemma 2 provides an efficient and feasible way of choosing $F_{\mathcal{T}}(\mathbf{t})$.

Lemma 2. *If \mathcal{X} and \mathcal{Y} are supported on a finite interval $[-1, 1]$, $\mathcal{C}_{\mathcal{T}}(\mathcal{X}, \mathcal{Y})$ in (4) is still a distance metric for distinguishing \mathcal{X} from \mathcal{Y} for any $F_{\mathcal{T}}(\mathbf{t})$ that samples \mathbf{t} within a small ball around $\mathbf{0}$.*

As will be introduced in the next section, we employ $\mathcal{C}_{\mathcal{T}}(\mathcal{X}, \mathcal{Y})$ as the loss to compare two distributions from the *critic*. By employing bounded activation functions (tanh, sigmoid, etc.), the requirement of Lemma 2 is automatically satisfied. Therefore, instead of searching within all the real distribution spaces, the choices of $F_{\mathcal{T}}(\mathbf{t})$ can be safely restricted to some zero-mean distributions, e.g., the Gaussian distribution. Furthermore, compared to the fixed Gaussian distribution, it is preferable that, whilst avoiding the ill-posed optimum, that $F_{\mathcal{T}}(\mathbf{t})$ could be optimised to better accommodate the difference between two distributions.

In this paper, we choose $F_{\mathcal{T}}(\mathbf{t})$ as the cdf of a broad class of distributions called the *scale mixture of normals*, in the form of

$$p_{\mathcal{T}}(\mathbf{t}) = \int_{\Sigma} p_{\mathcal{N}}(\mathbf{t}|\mathbf{0}, \Sigma) p_{\Sigma}(\Sigma) d\Sigma, \quad (7)$$

where $p_{\mathcal{T}}(\mathbf{t})$ is the pdf of $F_{\mathcal{T}}(\mathbf{t})$, while $p_{\mathcal{N}}(\mathbf{t}|\mathbf{0}, \Sigma)$ denotes the zero-mean Gaussian distribution with the covariance given by Σ , and $p_{\Sigma}(\Sigma)$ denotes distributions of Σ . It needs to be pointed out

that the *scale mixture of normals* constitutes a large portion of the elliptical distributions and includes many important distributions (e.g., the Gaussian, Cauchy, Student- t , hyperbolic distributions [39]) by choosing different $p_{\Sigma}(\Sigma)$. Therefore, instead of directly optimising $F_{\mathcal{T}}(\mathbf{t})$, which leads to ill-posed solutions, we alternatively optimise the neural net to output the samples of $p_{\Sigma}(\Sigma)$. By using the affine transformation (or the re-parametrisation trick), we are able to propagate back the gradients.

3 Reciprocal Adversarial Learning

3.1 Characteristic Function Loss in RCF-GAN

Although a valid and complete metric for measuring any forms of distributions, the CF loss in (4) works more efficiently and effectively in the embedded domain, than the data domain. To this end, we then express our RCF-GAN in the IPM-GAN format as

$$d(\mathcal{P}_d, \mathcal{P}_g) = \sup_{\mathcal{T}, f \in \mathcal{F}} \mathcal{C}_{\mathcal{T}}(f(\bar{\mathcal{X}}), f(\bar{\mathcal{Y}})), \quad \bar{\mathcal{X}} \sim \mathcal{P}_d \text{ and } \bar{\mathcal{Y}} \sim \mathcal{P}_g. \quad (8)$$

Lemma 3 below shows that this metric is well-defined for neural net training.

Lemma 3. *Given $f(\cdot)$ to be any differentiable function, the metric $\mathcal{C}_{\mathcal{T}}(f(\bar{\mathcal{X}}), f(\bar{\mathcal{Y}}))$ in (8) is bounded and differentiable almost everywhere.*

Because $\mathcal{C}_{\mathcal{T}}(f(\bar{\mathcal{X}}), f(\bar{\mathcal{Y}}))$ is bounded by construction, it relaxes the requirements on the *critic* $f \in \mathcal{F}$. Otherwise, we may need to bound \mathcal{F} to ensure the existence of the supremum [10]. Furthermore, having proved that $\mathcal{C}_{\mathcal{T}}(\mathcal{X}, \mathcal{Y}) = 0 \Leftrightarrow \mathcal{X} =^d \mathcal{Y}$, we also need to prove the equivalence between $\mathcal{C}_{\mathcal{T}}(f(\bar{\mathcal{X}}), f(\bar{\mathcal{Y}})) = 0$ and $\bar{\mathcal{X}} =^d \bar{\mathcal{Y}}$, to ensure that our RCF-GAN correctly learns the real distribution in the data domain. This is provided in Lemma 4.

Lemma 4. *Denote the distribution mapping by $\bar{\mathcal{Y}} =^d g(\mathcal{Z})$. Given two functions $f(\cdot)$ and $g(\cdot)$ that are reciprocal on the supports of $\bar{\mathcal{Y}}$ and \mathcal{Z} , that is, $\mathbb{E}_{\mathcal{Z}}[\|\mathbf{z} - f(g(\mathbf{z}))\|_2^2] = 0$, we also have $\mathbb{E}_{\bar{\mathcal{Y}}}[\|\bar{\mathbf{y}} - g(f(\bar{\mathbf{y}}))\|_2^2] = 0$. More importantly, this yields the following equivalences: $\mathcal{C}_{\mathcal{T}}(f(\bar{\mathcal{X}}), f(\bar{\mathcal{Y}})) = 0 \Leftrightarrow \mathcal{C}_{\mathcal{T}}(\bar{\mathcal{X}}, \bar{\mathcal{Y}}) = 0 \Leftrightarrow \mathcal{C}_{\mathcal{T}}(f(\bar{\mathcal{Y}}), \mathcal{Z}) = 0$ and $\mathcal{C}_{\mathcal{T}}(f(\bar{\mathcal{X}}), \mathcal{Z}) = 0$.*

3.2 Putting Everything Together: Latent Space Matching

Lemma 4 indicates that instead of being regarded as components of some IPMs (e.g., the W-GAN) to be optimised with strict restrictions, the *critic* can be basically regarded as feature mapping because in the embedded domain the CF loss is a valid distance metric of distributions. The *critic* can then be relaxed to satisfy the reciprocal property. Therefore, we incorporate the auto-encoder in only two modules by interchangeably treating the *critic* as the encoder and the generator as the decoder.

Remark 1. *Besides the computational ease, the structure of our RCF-GAN benefits both from the GAN and auto-encoder, as a way of unifying them. As an auto-encoder, the RCF-GAN enables to solely compare reconstructions in a meaningful embedded manifold instead of the data domain. When regarded as a GAN, the auto-encoder way theoretically and practically indicates the convergence; it also stabilises the training by pushing the embedded distributions to the Gaussian noise (i.e., \mathcal{Z}).*

In practice, in Lemma 4, we regard $f(\cdot)$ as the *critic* and $g(\cdot)$ as the generator. For the t -net, we denote it as $h(\cdot)$ and assume the covariance matrix of its output is diagonal (we thus represent it as σ), which is reasonable as in the embedded domain the multiple dimensions tend to be uncorrelated [40]. Moreover, the goal of the *critic* is to maximise (8) together with minimising an MSE loss to ensure the reciprocal property. Furthermore, to help our RCF-GAN in quickly mapping the real data distribution to the support of \mathcal{Z} , we further re-design the *critic* loss by finding an anchor as $\mathcal{C}_{\mathcal{T}}(f(\bar{\mathcal{Y}}), \mathcal{Z}) - \mathcal{C}_{\mathcal{T}}(f(\bar{\mathcal{X}}), \mathcal{Z})$. On the other hand, the generator is trained by minimising (8) as usual. The pseudo-code for our RCF-GAN is provided in Algorithm 1.

4 Experimental Results

In this section, our RCF-GAN is evaluated in terms of both random generations and reconstructions. We shall also point out that in this section, we report the results under the DCGAN structure [41] for a fair comparison with other GANs, however, our RCF-GAN may achieve even better performances by using, for example, residual blocks, a deeper t -net, tailored l_r in two scales, different weight α in (6), larger batch sizes or advanced techniques such as the spectral norm [9]. We report some of those

Algorithm 1: RCF-GAN. In all the experiments in this paper, we train the generator and the *critic* once at each iteration. We denote the optional *t*-net with parameter θ_t as $h_{\theta_t}(\cdot)$.

input: Real data distribution \mathcal{P}_d ; Gaussian noise $\mathcal{P}_\mathcal{N}$; batch sizes b_d, b_g, b_t and b_σ for the data, the generator input noise, \mathcal{T} and *t*-net input noise, respectively; learning rate l_r ; reciprocal regularisation in the embedded domain λ

output: Net parameters θ_c and θ_g for the *critic* and generator, respectively

while θ_c and θ_g not converge **do**

```

/* train the critic */
Sample from distributions:  $\{\bar{\mathbf{x}}_i\}_{i=1}^{b_d} \sim \mathcal{P}_d; \{\mathbf{z}_i\}_{i=1}^{b_g} \sim \mathcal{P}_\mathcal{N}; \{\mathbf{t}_i\}_{i=1}^{b_t} \sim \mathcal{P}_\mathcal{N}; \{\sigma_i\}_{i=1}^{b_\sigma} \sim \mathcal{P}_\mathcal{N}$ 
Affine transform:  $\{\mathbf{t}_i\}_{i=1}^{b_t} \leftarrow (\{\mathbf{t}_i\}_{i=1}^{b_t}, h_{\theta_t}(\{\sigma_i\}_{i=1}^{b_\sigma}))$  // optional
Calculate adversarial loss: // empirical version of  $\mathcal{C}_\mathcal{T}(f(\bar{\mathcal{Y}}), \mathcal{Z}) - \mathcal{C}_\mathcal{T}(f(\bar{\mathcal{X}}), \mathcal{Z})$ 
 $\mathcal{L} = \mathcal{C}_{\{\mathbf{t}_i\}_{i=1}^{b_t}}(f_{\theta_c}(g_{\theta_g}(\{\mathbf{z}_i\}_{i=1}^{b_g})), \{\mathbf{z}_i\}_{i=1}^{b_g}) - \mathcal{C}_{\{\mathbf{t}_i\}_{i=1}^{b_t}}(f_{\theta_c}(\{\bar{\mathbf{x}}_i\}_{i=1}^{b_d}), \{\mathbf{z}_i\}_{i=1}^{b_g})$ 
Update:  $\theta_t \leftarrow \theta_t + l_r \cdot \text{Adam}(\theta_t, \nabla_{\theta_t}[-\mathcal{L}])$ 
 $\theta_c \leftarrow \theta_c + l_r \cdot \text{Adam}(\theta_c, \nabla_{\theta_c}[-\mathcal{L} + \lambda \sum_{i=1}^{b_g} \|\mathbf{z}_i - f_{\theta_g}(g_{\theta_g}(\mathbf{z}_i))\|_2^2])$ 
/* train the generator */
Sample from distributions:  $\{\bar{\mathbf{x}}_i\}_{i=1}^{b_d} \sim \mathcal{P}_d; \{\mathbf{z}_i\}_{i=1}^{b_g} \sim \mathcal{P}_\mathcal{N}; \{\mathbf{t}_i\}_{i=1}^{b_t} \sim \mathcal{P}_\mathcal{N}; \{\sigma_i\}_{i=1}^{b_\sigma} \sim \mathcal{P}_\mathcal{N}$ 
Affine transform:  $\{\mathbf{t}_i\}_{i=1}^{b_t} \leftarrow (\{\mathbf{t}_i\}_{i=1}^{b_t}, h_{\theta_t}(\{\sigma_i\}_{i=1}^{b_\sigma}))$  // optional
Calculate adversarial loss: // empirical version of  $\mathcal{C}_\mathcal{T}(f(\bar{\mathcal{Y}}), f(\bar{\mathcal{X}}))$ 
 $\mathcal{L} = \mathcal{C}_{\{\mathbf{t}_i\}_{i=1}^{b_t}}(f_{\theta_c}(g_{\theta_g}(\{\mathbf{z}_i\}_{i=1}^{b_g})), f_{\theta_c}(\{\bar{\mathbf{x}}_i\}_{i=1}^{b_d}))$ 
Update:  $\theta_g \leftarrow \theta_g + l_r \cdot \text{Adam}(\theta_g, \nabla_{\theta_g}[\mathcal{L}])$ 

```

Table 1: The FID and KID scores under the DCGAN structure. The results of the DCGAN and W-GAN-GP are from [29] and [14]. The official codes were run to obtain the results of the W-GAN [5] and MMD-GAN [13]. The results of the AGE were tested from its pre-trained models [20].

Methods	FID			KID		
	CIFAR-10	Celeba	LSUN_B	CIFAR-10	Celeba	LSUN_B
DCGAN	37.7 [29]	21.4 [29]	70.4 [29]	—	—	—
W-GAN	42.64±0.263	31.85±0.275	57.05±0.368	0.025±0.001	0.023±0.001	0.048±0.002
W-GAN-GP	37.52±0.19[14]	—	41.39±0.25[14]	0.026±0.001[14]	—	0.039±0.002[14]
MMD-GAN	42.8±0.272	32.5±0.161	56.52±0.338	0.025±0.001	0.024±0.001	0.047±0.002
AGE	32.54±0.238	23.19±0.136	—	0.020±0.001	0.017±0.001	—
RCF-GAN _(t_norm)	31.55±0.197	19.34±0.215	38.16±0.286	0.019±0.001	0.012±0.001	0.032±0.001
RCF-GAN _(t_net)	31.21±0.207	15.86±0.075	40.15±0.403	0.018±0.001	0.011±0.001	0.034±0.001
AGE(R)	47.37±0.318	30.77±0.186	—	0.022±0.001	0.024±0.001	—
RCF-GAN _(t_net) (R)	28.70±0.156	14.82±0.118	44.16±0.421	0.014±0.001	0.009±0.000	0.036±0.001

Note: (R) means the FID and KID scores for the reconstructed images.

improvements in the supplementary material, including the achieved state-of-the-art results by using the residual nets. Our code will be released at https://github.com/ShengxiLi/rcf_gan.

Datasets: Three widely applied benchmark datasets were employed in our evaluation: CelebA (faces of celebrity) [42], CIFAR10 [43] and LSUN Bedroom (LSUN_B) [44]. The images of the CelebA and LSUN_B were central cropped to the size 64×64 , whilst the image size of the CIFAR10 was 32×32 . Furthermore, when evaluating the reconstruction, the test sets of the CIFAR10 and LSUN_B were employed, from which the samples were not used in the training.

Baselines: As our work is mainly related to the IPM-GANs, we compared our RCF-GAN with the W-GAN [5], W-GAN with gradient penalty (W-GAN-GP) [8] and MMD-GAN [13, 14]. For image reconstruction, we compared our RCF-GAN with the recent adversarial generator-encoder (AGE) work [20], which empirically performs better than the adversarially learned inference (ALI) [26].

Metrics: We employed the Fréchet inception distance (FID) [29], which is basically the Wasserstein distance between two Gaussian distributions, together with the kernel inception distance (KID) that arises from the MMD metric [14].

Net structure and technical details: For a fair comparisons, all the reported results were compared under the batch sizes of 64 (i.e., $b_d = b_g = b_t = b_\sigma = 64$) and also based on the network structure being

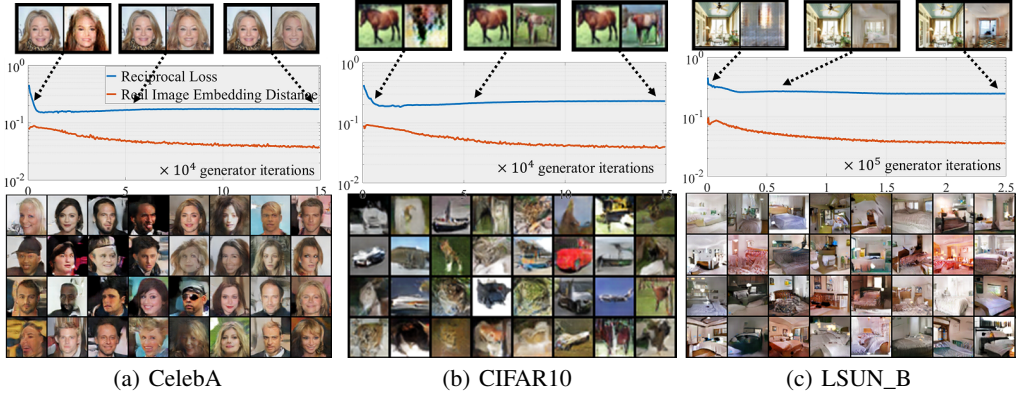


Figure 3: The convergence curves and images generated by our RCF-GAN from Gaussian noise.



Figure 4: The images reconstructed by our RCF-GAN(t_{net}), AGE and MMD-GAN in the CelebA dataset. The upper panel shows the reconstructed images (on the right hand side of each pair) corresponding to the original images (on the left hand side of each pair). The lower panel displays the linear interpolation in the embedded domain.

the same as that in the DCGAN [41], without any extra layers. In our RCF-GAN, we set λ to linearly space from 0.6 to 1, which is reasonable as the role of *critic* changes from a discriminator to an encoder along the training procedure. Moreover, we set all variances of Gaussian noise to 1, except for the input noise of the generator that was 0.3, because the reciprocal loss has to be minimised given the fact that the output of the *critic* is restricted to $[-1, 1]$. Furthermore, we do not require the Lipschitz constraint, which allows for a larger learning rate ($l_r = 0.0002$ for both nets). Moreover, for the CIFAR10 and LSUN_B datasets, the dimension of the embedded domain was set to 128 and for the CelebA dataset the dimension was 64. The optional t -net, if used, was a small three layer fully connected net, with the dimension of each layer being the same as the embedded dimension.

Image generation: The generated images from random Gaussian noise are shown in Fig. 3. Observe that by using our proposed CF loss in the RCF-GAN, the generated images are clear and close to the real images. We further provide the FID and KID scores in Table 1. This table shows that our RCF-GAN consistently achieved the best performances across the three datasets. More importantly, employing the t -net in outputting optimal $F_{\mathcal{T}}(\mathbf{t})$ is beneficial, where further improvements are achieved. We also found that using the t -net resulted in better reconstructed images. More importantly, compared to a fluctuated generator loss that is caused by the adversarial module in GANs, we take the advantages of the auto-encoder structure in utilising the reciprocal loss (i.e., $\mathbb{E}_{\mathcal{Z}}[\|\mathbf{z} - f(g(\mathbf{z}))\|_2^2]$ indicates the reciprocal, and the distance between the fake embedded and the Gaussian distributions), together with the distance between the embedded real distribution $f(\mathcal{X})$ and the Gaussian distribution \mathcal{Z} (i.e., $\mathcal{C}_{\mathcal{T}}(f(\mathcal{X}), \mathcal{Z})$) to better indicate the convergence, which are shown in Figure 3. The reciprocal loss basically measures the convergence on reconstructions, whereas the real image embedding distance $\mathcal{C}_{\mathcal{T}}(f(\mathcal{X}), \mathcal{Z})$ indicates the performance on generating images.

Image reconstruction: The images reconstructed from the original images are shown in Fig. 4. Because our RCF-GAN only matches the distributions in the embedded domain, the reconstructed

images are thus clear and semantically meaningful, resulting in a meaningful interpolation in Fig. 4. This is beneficial because rather than randomly generating real images, our RCF-GAN is able to bi-directionally reconstruct and interpolate real images. In contrast, although MMD-GANs employ a third module to achieve an auto-encoder, the decoded images are severely blurred. In the last three rows of Table 1, we can also see that the images reconstructed by our RCF-GAN are superior to those from the AGE. More importantly, the images from our RCF-GAN are consistently superior, whilst the quality of the reconstructed images in the AGE is much inferior to its random generated images. This also indicates the effectiveness of the unified structure of our RCF-GAN.

5 Conclusion

We have introduced an efficient generative adversarial net (GAN) structure that seamlessly combines the IPM-GANs and auto-encoders. In this way, the reciprocal in our RCF-GAN ensures the equivalence between the embedded and data domains, whereas in the embedded domain the comparison on two distributions is strongly supported by the proposed powerful characteristic function (CF) loss, together with the physically meaningful phase and amplitude information, and an efficient sampling strategy. The reciprocal has been shown to also stabilise the convergence of the adversarial learning in our RCF-GAN, and at the same time to benefit from meaningful comparisons in the embedded domain. Consequently, the experimental results have demonstrated the superior performances of our RCF-GAN in both generating images and reconstructing images.

6 Broader Impact

A combination of the auto-encoder and GANs has been extensively studied, and has been shown to achieve a broader data generation and reconstruction. The RCF-GAN proposed in this paper provides a neat and new structure in the combination. The studies of GANs and those design on probabilistic auto-encoders basically start from different perspectives because the former serves for the generation, or it “decodes” from random noise, whilst the latter, as its name implies, focuses on encoding to summarise information. Although there are extensive attempts on combining those two structures, they typically embed one into the other as components such as by using an auto-encoder as a discriminator in GANs or using an adversarial idea in an auto-encoder. This paper provides a way of equally treating the two structures; the proposed structure, which contains only two modules, can be regarded both as an “encoder-decoder” and “discriminator-generator”. The proposed combination benefits both, that is, it equips an auto-encoder the ability to meaningfully encode via matching in the embedded domain, whilst ensuring the convergence of the adversarial as a GAN.

Moreover, instead of being a component to measure the distance as in the W-GAN, regarding the *critic* as an independent feature mapping module with a sufficient distance metric is beneficial to allow learning in the embedded domain for any types of feature extraction models, such as the deep canonical correlation analysis net and graph auto encoder. A large amount of unsupervised learning models, then, can be connected and improved with the adversarial learning.

Another potential benefit of our work is to bring the general concept of the characteristic function (CF) into practice, by providing efficient sampling methods. The CF has been previously studied as a powerful tool in theoretical probabilistic analysis, while its practical applications have been limited due to complex functional forms. We should also highlight the physical meaning of the CF components introduced in this paper. It is a well known experimental phenomenon that the phase of discrete Fourier transform of images captures the saliency information, which motivates a large volume of works in saliency detection. This paper gives a probabilistic explanation to this, paving the way for future work to embark upon this intrinsic relationship.

References

- [1] Ian Goodfellow, Jean Pouget-Abadie, Mehdi Mirza, Bing Xu, David Warde-Farley, Sherjil Ozair, Aaron Courville, and Yoshua Bengio. Generative adversarial nets. In *Advances in Neural Information Processing Systems*, pages 2672–2680, 2014.
- [2] Lars Mescheder, Andreas Geiger, and Sebastian Nowozin. Which training methods for GANs do actually converge? *arXiv preprint arXiv:1801.04406*, 2018.
- [3] Martín Arjovsky and Léon Bottou. Towards principled methods for training generative adversarial networks. *ArXiv*, abs/1701.04862, 2017.

- [4] Alfred Müller. Integral probability metrics and their generating classes of functions. *Advances in Applied Probability*, 29(2):429–443, 1997.
- [5] Martin Arjovsky, Soumith Chintala, and Léon Bottou. Wasserstein GAN. *arXiv preprint arXiv:1701.07875*, 2017.
- [6] Sanjeev Arora, Rong Ge, Yingyu Liang, Tengyu Ma, and Yi Zhang. Generalization and equilibrium in generative adversarial nets (GANs). In *Proceedings of the 34th International Conference on Machine Learning*, pages 224–232. JMLR. org, 2017.
- [7] Sanjeev Arora and Yi Zhang. Do GANs actually learn the distribution? An empirical study. *arXiv preprint arXiv:1706.08224*, 2017.
- [8] Ishaan Gulrajani, Faruk Ahmed, Martin Arjovsky, Vincent Dumoulin, and Aaron C Courville. Improved training of Wasserstein GANs. In *Advances in Neural Information Processing Systems*, pages 5767–5777, 2017.
- [9] Takeru Miyato, Toshiki Kataoka, Masanori Koyama, and Yuichi Yoshida. Spectral normalization for generative adversarial networks. *arXiv preprint arXiv:1802.05957*, 2018.
- [10] Youssef Mroueh and Tom Sercu. Fisher GAN. In *Advances in Neural Information Processing Systems*, pages 2513–2523, 2017.
- [11] Youssef Mroueh, Tom Sercu, and Vaibhava Goel. McGAN: Mean and covariance feature matching gan. *arXiv preprint arXiv:1702.08398*, 2017.
- [12] Sung Woo Park and Junseok Kwon. Sphere generative adversarial network based on geometric moment matching. In *Proceedings of the IEEE Conference on Computer Vision and Pattern Recognition*, pages 4292–4301, 2019.
- [13] Chun-Liang Li, Wei-Cheng Chang, Yu Cheng, Yiming Yang, and Barnabás Póczos. MMD gan: Towards deeper understanding of moment matching network. In *Advances in Neural Information Processing Systems*, pages 2203–2213, 2017.
- [14] Mikołaj Bińkowski, Dougal J Sutherland, Michael Arbel, and Arthur Gretton. Demystifying MMD GANs. *arXiv preprint arXiv:1801.01401*, 2018.
- [15] Farzan Farnia and David Tse. A convex duality framework for GANs. In *Advances in Neural Information Processing Systems*, pages 5248–5258, 2018.
- [16] Shuang Liu, Olivier Bousquet, and Kamalika Chaudhuri. Approximation and convergence properties of generative adversarial learning. In *Advances in Neural Information Processing Systems*, pages 5545–5553, 2017.
- [17] Shakir Mohamed and Balaji Lakshminarayanan. Learning in implicit generative models. *arXiv preprint arXiv:1610.03483*, 2016.
- [18] Youssef Mroueh, Chun-Liang Li, Tom Sercu, Anant Raj, and Yu Cheng. Sobolev GAN. *arXiv preprint arXiv:1711.04894*, 2017.
- [19] Shengxi Li, Zeyang Yu, Min Xiang, and Danilo Mandic. Solving general elliptical mixture models through an approximate Wasserstein manifold. *arXiv preprint arXiv:1906.03700*, 2019.
- [20] Dmitry Ulyanov, Andrea Vedaldi, and Victor Lempitsky. It takes (only) two: Adversarial generator-encoder networks. In *Thirty-Second AAAI Conference on Artificial Intelligence*, 2018.
- [21] Alireza Makhzani, Jonathon Shlens, Navdeep Jaitly, Ian Goodfellow, and Brendan Frey. Adversarial autoencoders. *arXiv preprint arXiv:1511.05644*, 2015.
- [22] Anders Boesen Lindbo Larsen, Søren Kaae Sønderby, Hugo Larochelle, and Ole Winther. Autoencoding beyond pixels using a learned similarity metric. *arXiv preprint arXiv:1512.09300*, 2015.
- [23] Jeff Donahue, Philipp Krähenbühl, and Trevor Darrell. Adversarial feature learning. *arXiv preprint arXiv:1605.09782*, 2016.
- [24] Andrew Brock, Theodore Lim, James M Ritchie, and Nick Weston. Neural photo editing with introspective adversarial networks. *arXiv preprint arXiv:1609.07093*, 2016.
- [25] Tong Che, Yanran Li, Athul Paul Jacob, Yoshua Bengio, and Wenjie Li. Mode regularized generative adversarial networks. *arXiv preprint arXiv:1612.02136*, 2016.

- [26] Vincent Dumoulin, Ishmael Belghazi, Ben Poole, Olivier Mastropietro, Alex Lamb, Martin Arjovsky, and Aaron Courville. Adversarially learned inference. *arXiv preprint arXiv:1606.00704*, 2016.
- [27] Abdul Fatir Ansari, Jonathan Scarlett, and Harold Soh. A characteristic function approach to deep implicit generative modeling. In *IEEE Conference on Computer Vision and Pattern Recognition*, 2020.
- [28] Tero Karras, Timo Aila, Samuli Laine, and Jaakko Lehtinen. Progressive growing of GANs for improved quality, stability, and variation. *arXiv preprint arXiv:1710.10196*, 2017.
- [29] Martin Heusel, Hubert Ramsauer, Thomas Unterthiner, Bernhard Nessler, and Sepp Hochreiter. GANs trained by a two time-scale update rule converge to a local Nash equilibrium. In *Advances in Neural Information Processing Systems*, pages 6626–6637, 2017.
- [30] David Williams. *Probability with martingales*. Cambridge University Press, 1991.
- [31] Andrey Feuerverger, Roman A Mureika, et al. The empirical characteristic function and its applications. *The Annals of Statistics*, 5(1):88–97, 1977.
- [32] Eugene Lukacs. A survey of the theory of characteristic functions. *Advances in Applied Probability*, 4(1): 1–37, 1972.
- [33] TW Epps and Kenneth J Singleton. An omnibus test for the two-sample problem using the empirical characteristic function. *Journal of Statistical Computation and Simulation*, 26(3–4):177–203, 1986.
- [34] Kacper P Chwialkowski, Aaditya Ramdas, Dino Sejdinovic, and Arthur Gretton. Fast two-sample testing with analytic representations of probability measures. In *Advances in Neural Information Processing Systems*, pages 1981–1989, 2015.
- [35] Kai Wang Fang. *Symmetric multivariate and related distributions*. CRC Press, 2018.
- [36] Sergei Germanovich Bobkov. Proximity of probability distributions in terms of Fourier–Stieltjes transforms. *Russian Mathematical Surveys*, 71(6):1021, 2016.
- [37] Zeyang Yu, Shengxi Li, and Danilo Mandic. Widely linear complex-valued autoencoder: Dealing with noncircularity in generative-discriminative models. In *International Conference on Artificial Neural Networks*, pages 339–350. Springer, 2019.
- [38] Bharath K Sriperumbudur, Arthur Gretton, Kenji Fukumizu, Bernhard Schölkopf, and Gert RG Lanckriet. Hilbert space embeddings and metrics on probability measures. *Journal of Machine Learning Research*, 11 (Apr):1517–1561, 2010.
- [39] David F Andrews and Colin L Mallows. Scale mixtures of normal distributions. *Journal of the Royal Statistical Society: Series B (Methodological)*, 36(1):99–102, 1974.
- [40] Diederik P Kingma and Max Welling. Auto-encoding variational bayes. *arXiv preprint arXiv:1312.6114*, 2013.
- [41] Alec Radford, Luke Metz, and Soumith Chintala. Unsupervised representation learning with deep convolutional generative adversarial networks. *arXiv preprint arXiv:1511.06434*, 2015.
- [42] Ziwei Liu, Ping Luo, Xiaogang Wang, and Xiaoou Tang. Deep learning face attributes in the wild. In *Proceedings of the IEEE International Conference on Computer Vision*, pages 3730–3738, 2015.
- [43] Alex Krizhevsky, Geoffrey Hinton, et al. Learning multiple layers of features from tiny images. 2009.
- [44] Fisher Yu, Ari Seff, Yinda Zhang, Shuran Song, Thomas Funkhouser, and Jianxiong Xiao. Lsun: Construction of a large-scale image dataset using deep learning with humans in the loop. *arXiv preprint arXiv:1506.03365*, 2015.
- [45] Carl-Gustav Esseen et al. Fourier analysis of distribution functions: A mathematical study of the Laplace-Gaussian law. *Acta Mathematica*, 77:1–125, 1945.
- [46] K. Kreutz-Delgado. The complex gradient operator and the CR-calculus. *arXiv preprint arXiv:0906.4835*, 2009.
- [47] D. P. Mandic and V. S. L. Goh. *Complex valued nonlinear adaptive filters: Noncircularity, widely linear and neural models*, volume 59. John Wiley & Sons, 2009.

- [48] Marc G Bellemare, Ivo Danihelka, Will Dabney, Shakir Mohamed, Balaji Lakshminarayanan, Stephan Hoyer, and Rémi Munos. The Cramer distance as a solution to biased Wasserstein gradients. *arXiv preprint arXiv:1705.10743*, 2017.
- [49] David Berthelot, Thomas Schumm, and Luke Metz. Began: Boundary equilibrium generative adversarial networks. *arXiv preprint arXiv:1703.10717*, 2017.
- [50] Ishan Deshpande, Ziyu Zhang, and Alexander G Schwing. Generative modeling using the sliced Wasserstein distance. In *Proceedings of the IEEE Conference on Computer Vision and Pattern Recognition*, pages 3483–3491, 2018.

Appendices

A Additional and State-of-the-art Results

We evaluated the effectiveness and robustness of our RCF-GAN in two additional net structures, i.e., advanced DCGAN (adv-DCGAN) and residual net (ResNet) structures. In the adv-DCGAN structure, we increased the size of the generator whilst keeping the discriminator the same as that in the original DCGAN. For the ResNet structure, we adopted the same structure proposed in [8]. We illustrate the difference between the generators of the adv-DCGAN and the original DCGAN in the following.

DCGAN: Generator for image size 64×64 $\mathbf{z} \in \mathbb{R}^{64}$ for CelebA and $\mathbf{z} \in \mathbb{R}^{128}$ for LSUN_B ConvTrans(channel=512, kernel=4, stride=1, pad=0) BatchNorm and Relu ConvTrans(channel=256, kernel=4, stride=2, pad=1) BatchNorm and Relu ConvTrans(channel=128, kernel=4, stride=2, pad=1) BatchNorm and Relu ConvTrans(channel=64, kernel=4, stride=2, pad=1) BatchNorm and Relu ConvTrans(channel=3, kernel=4, stride=2, pad=1) Tanh	Adv-DCGAN: Generator for image size 64×64 $\mathbf{z} \in \mathbb{R}^{64}$ for CelebA and $\mathbf{z} \in \mathbb{R}^{128}$ for LSUN_B ConvTrans(channel=1024, kernel=4, stride=1, pad=0) BatchNorm and Relu ConvTrans(channel=512, kernel=4, stride=2, pad=1) BatchNorm and Relu ConvTrans(channel=256, kernel=4, stride=2, pad=1) BatchNorm and Relu ConvTrans(channel=128, kernel=4, stride=2, pad=1) BatchNorm and Relu ConvTrans(channel=3, kernel=4, stride=2, pad=1) Tanh
DCGAN: Generator for image size 32×32 $\mathbf{z} \in \mathbb{R}^{128}$ for CIFAR10 ConvTrans(channel=256, kernel=4, stride=1, pad=0) BatchNorm and Relu ConvTrans(channel=128, kernel=4, stride=2, pad=1) BatchNorm and Relu ConvTrans(channel=64, kernel=4, stride=2, pad=1) BatchNorm and Relu ConvTrans(channel=3, kernel=4, stride=2, pad=1) Tanh	Adv-DCGAN: Generator for image size 32×32 $\mathbf{z} \in \mathbb{R}^{128}$ for CIFAR10 ConvTrans(channel=512, kernel=4, stride=1, pad=0) BatchNorm and Relu ConvTrans(channel=256, kernel=4, stride=2, pad=1) BatchNorm and Relu ConvTrans(channel=128, kernel=4, stride=2, pad=1) BatchNorm and Relu ConvTrans(channel=3, kernel=4, stride=2, pad=1) Tanh

Moreover, for the results on the DCGAN structure (reported in the paper), we trained our RCF-GAN for 150K iterations for both the CelebA and the CIFAR10 datasets, whereby 250K iterations were set to the LSUN_B dataset. However, in the two additional structures (reported in the supplementary material), we set the maximum number of iterations to 100K for all the datasets, and also set the regulator fixed to $\lambda = 0.8$ for simplicity. Although increasing the number of iterations and using linearly spaced λ can gain further improvements, the achieved results are already the state-of-the-art, which is enough to validate the superior performances in bi-directionally generating clear images of our RCF-GAN. We report the overall results by extending the results of the paper in Table 2.

We can easily see that under the adv-DCGAN structure, our RCF-GAN consistently and stably achieved improvements by using a deeper generator. However, because the structure of the *critic* in the adv-DCGAN is the same as that in the DCGAN, the reconstruction quality of our RCF-GAN under the adv-DCGAN structure is comparable to that under the DCGAN structure. Furthermore, as proposed in [8], the ResNet structure has been

Table 2: The FID and KID scores under the DCGAN structure. The results of the DCGAN and W-GAN-GP are from [29] and [14]. The official codes were run to obtain the results of the W-GAN [5] and MMD-GAN [13]. The results of the AGE were tested from its pre-trained models [20]. We use RCF-GAN* to represent our RCF-GAN trained under the adv-DCGAN structure.

Methods	FID			KID		
	CIFAR-10	Celeba	LSUN_B	CIFAR-10	Celeba	LSUN_B
DCGAN	37.7 [29]	21.4 [29]	70.4 [29]	—	—	—
W-GAN	42.64±0.263	31.85±0.275	57.05±0.368	0.025±0.001	0.023±0.001	0.048±0.002
W-GAN-GP	37.52±0.19[14]	—	41.39±0.25[14]	0.026±0.001[14]	—	0.039±0.002[14]
MMD-GAN	42.80±0.272	32.5±0.161	56.52±0.338	0.025±0.001	0.024±0.001	0.047±0.002
AGE	32.54±0.238	23.19±0.136	—	0.020±0.001	0.017±0.001	—
RCF-GAN _(t_norm)	31.55±0.197	19.34±0.215	38.16±0.286	0.019±0.001	0.012±0.001	0.032±0.001
RCF-GAN _(t_net)	31.21±0.207	15.86±0.075	40.15±0.403	0.018±0.001	0.011±0.001	0.034±0.001
RCF-GAN* _(t_net)	31.20±0.179	13.75±0.125	36.02±0.241	0.018±0.001	0.009±0.000	0.030±0.001
AGE(R)	47.37±0.318	30.77±0.186	—	0.022±0.001	0.024±0.001	—
RCF-GAN _(t_net) (R)	28.70±0.156	14.82±0.118	44.16±0.421	0.014±0.001	0.009±0.000	0.036±0.001
RCF-GAN* _(t_net) (R)	26.51±0.223	12.71±0.119	49.42±0.378	0.012±0.001	0.008±0.000	0.041±0.002

Note: (R) means the FID and KID scores for the reconstructed images.

utilised in training the LSUN_B dataset. We thus report in Table 3 the comparisons under the ResNet structure, which is relatively larger in both the sizes of the generator and the *critic*, compared to the adv-DCGAN and DCGAN structures.

Table 3: The FID and KID scores evaluated on the LSUN_B dataset. The results of the DCGAN and W-GAN-GP are from [29] and [14] under the DCGAN structure. We also report the result of the Sphere-GAN under the ResNet structure [12]. The official codes were run to obtain the results of the W-GAN [5] and MMD-GAN [13] under the DCGAN structure. We use RCF-GAN[†] to represent the proposed RCF-GAN trained under the ResNet structure.

Methods	FID	KID
DCGAN	70.4 [29]	—
W-GAN	57.05±0.368	0.048±0.002
W-GAN-GP	41.39±0.25[14]	0.039±0.002[14]
MMD-GAN	56.52±0.338	0.047±0.002
Sphere-GAN	16.9[12]	—
RCF-GAN [†] _(t_net)	16.25±0.166	0.010±0.001
RCF-GAN [†] _(t_net) (R)	11.42±0.117	0.005±0.000

Note: (R) means the FID and KID scores for the reconstructed images.

In the following, we show the subjective results of the generation and reconstruction by our RCF-GAN.

B Proofs

Proof of Lemma 1: We here prove the non-negativity, symmetry and triangle properties that are required as a valid distance metric in the following.

Non-negativity: Based on the definition of $\mathcal{C}_{\mathcal{T}}(\mathcal{X}, \mathcal{Y})$,

$$\mathcal{C}_{\mathcal{T}}(\mathcal{X}, \mathcal{Y}) = \int_{\mathbf{t}} \underbrace{((\Phi_{\mathcal{X}}(\mathbf{t}) - \Phi_{\mathcal{Y}}(\mathbf{t}))(\Phi_{\mathcal{X}}^*(\mathbf{t}) - \Phi_{\mathcal{Y}}^*(\mathbf{t})))}_{c(\mathbf{t})}^{1/2} dF_{\mathcal{T}}(\mathbf{t}), \quad (9)$$

the term $\mathcal{C}_{\mathcal{T}}(\mathcal{X}, \mathcal{Y})$ is non-negative because $c(\mathbf{t}) \geq 0$ for all \mathbf{t} . We next prove when the equality holds.

- $\mathcal{X} =^d \mathcal{Y} \rightarrow \mathcal{C}_{\mathcal{T}}(\mathcal{X}, \mathcal{Y}) = 0$: This is evident because $\Phi_{\mathcal{X}}(\mathbf{t}) = \Phi_{\mathcal{Y}}(\mathbf{t})$ for all \mathbf{t} .
- $\mathcal{X} =^d \mathcal{Y} \leftarrow \mathcal{C}_{\mathcal{T}}(\mathcal{X}, \mathcal{Y}) = 0$: Given that the support of \mathcal{T} is \mathbb{R}^m , $\int_{\mathbf{t}} \sqrt{c(\mathbf{t})} dF_{\mathcal{T}}(\mathbf{t}) = 0$ exists if and only if $c(\mathbf{t}) = 0$ everywhere. Therefore, $\Phi_{\mathcal{X}}(\mathbf{t}) = \Phi_{\mathcal{Y}}(\mathbf{t})$ for all $\mathbf{t} \in \mathbb{R}^m$. According to the *Uniqueness Theorem* of the CF, we have $\mathcal{X} =^d \mathcal{Y}$.

Therefore, we have that $\mathcal{C}_{\mathcal{T}}(\mathcal{X}, \mathcal{Y}) \geq 0$, and the equality holds if and only if $\mathcal{X} =^d \mathcal{Y}$.

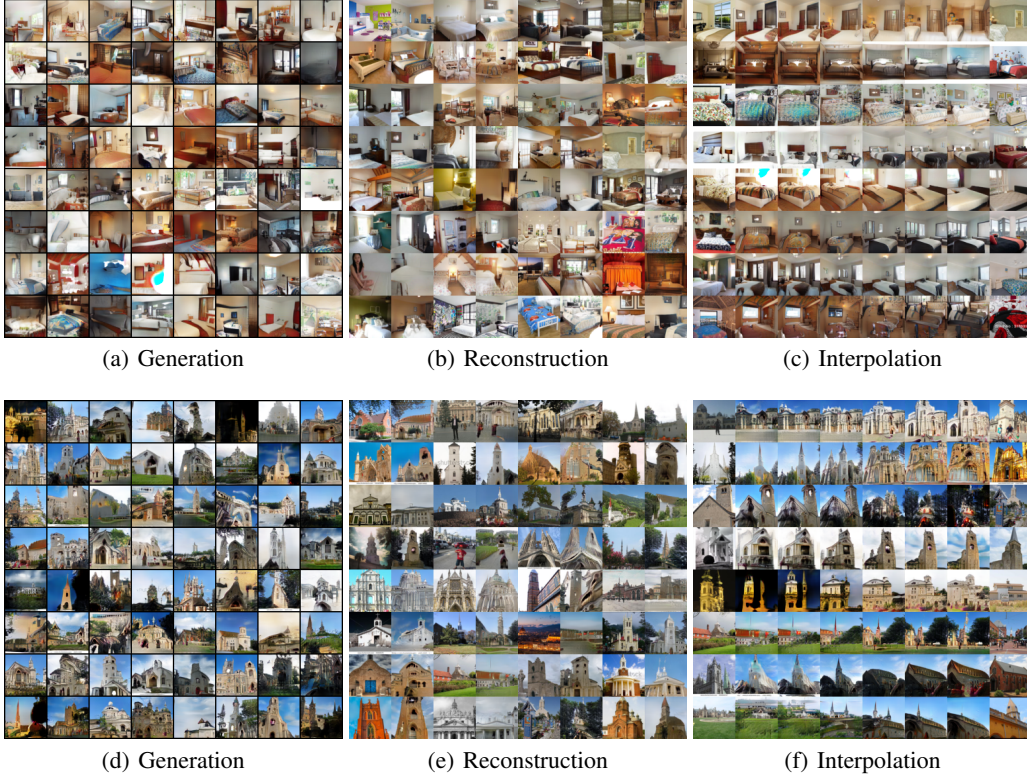


Figure 5: Images generated, reconstructed and interpolated by our RCF-GAN under the ResNet structure. Note that in (b) and (e), the reconstructed images are shown on the right hand side of each pair whereas the corresponding original images are on the left hand side of each pair.

Symmetry: This is obvious for the symmetry of $c(t)$, thus yielding $\mathcal{C}_{\mathcal{T}}(\mathcal{X}, \mathcal{Y}) = \mathcal{C}_{\mathcal{T}}(\mathcal{Y}, \mathcal{X})$.

Triangle: Because the CFs $\Phi_{\mathcal{X}}(t)$ and $\Phi_{\mathcal{Z}}(t)$ are the elements of the normed vector space, we have the following inequality (also known as the Minkowski inequality),

$$\begin{aligned} \int_t |\Phi_{\mathcal{X}}(t) - \Phi_{\mathcal{Z}}(t) + \Phi_{\mathcal{Z}}(t) - \Phi_{\mathcal{Y}}(t)| dF_{\mathcal{T}}(t) \\ \leq \int_t |\Phi_{\mathcal{X}}(t) - \Phi_{\mathcal{Z}}(t)| dF_{\mathcal{T}}(t) + \int_t |\Phi_{\mathcal{Z}}(t) - \Phi_{\mathcal{Y}}(t)| dF_{\mathcal{T}}(t). \end{aligned} \quad (10)$$

Therefore, the triangle property of $\mathcal{C}_{\mathcal{T}}(\mathcal{X}, \mathcal{Y})$ follows as

$$\mathcal{C}_{\mathcal{T}}(\mathcal{X}, \mathcal{Y}) \leq \mathcal{C}_{\mathcal{T}}(\mathcal{X}, \mathcal{Z}) + \mathcal{C}_{\mathcal{T}}(\mathcal{Z}, \mathcal{Y}). \quad (11)$$

Therefore, $\mathcal{C}_{\mathcal{T}}(\mathcal{X}, \mathcal{Y})$ is a valid distance metric in measuring discrepancies between two random variables \mathcal{X} and \mathcal{Y} .

This completes the proof.

Proof of Lemma 2: The proof of the triangle and symmetry properties is the same as those in Lemma 1. The non-negativity is also evident and the same as that in Lemma 1 but the equality holds for different conditions. We provide its proof in the following.

Before introducing our proof, we first quote Theorem 3 from Essen [45].

Theorem 3 ([45]) *The distributions of two random variables \mathcal{X} and \mathcal{Y} are the same when*

- $\Phi_{\mathcal{X}}(t) = \Phi_{\mathcal{Y}}(t)$ in an interval around $\mathbf{0}$;
- $\beta_k = \int_x x^k dF_{\mathcal{X}}(x) < \infty$ for $k = 0, 1, 2, 3, \dots$
- $\sum_{k=1}^{\infty} 1/\beta_{2k}^{1/2k}$ diverges, which means that the moment problem of β_k is determined and unique.

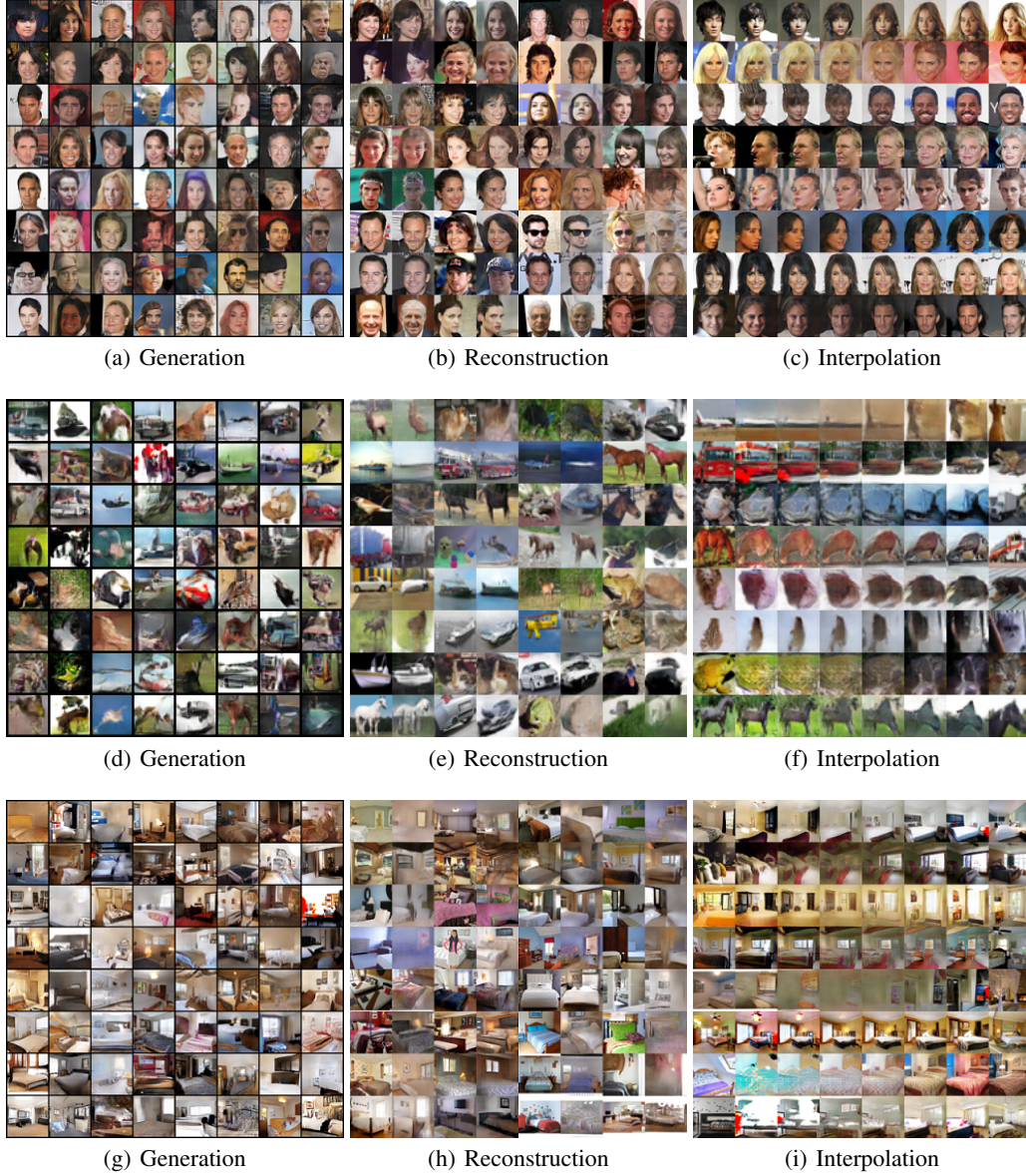


Figure 6: Images generated, reconstructed and interpolated by our RCF-GAN under the adv-DCGAN structure. Note that in (b), (e) and (h), the reconstructed images are shown on the right hand side of each pair whereas the corresponding original images are on the left hand side of each pair.

It is the fact that only requiring $\Phi_{\mathcal{X}}(\mathbf{t}) = \Phi_{\mathcal{Y}}(\mathbf{t})$ in an interval around $\mathbf{0}$ does not ensure the equivalence between two distributions without any other constraints, given the counterexample provided in [45] as well. This equivalence even cannot be ensured when all the moments are matched. The third condition, intuitively, guarantees this equivalence by restricting that the moment does not increase “extremely” fast when $k \rightarrow \infty$.

In Lemma 2 of this paper, we bound \mathcal{X} and \mathcal{Y} by $[-1, 1]$, thus having $|\beta_k| \leq 1 < \infty$ and $1/\beta_{2k}^{1/2k} \geq 1$ so that $\sum_{k=1}^{\infty} 1/\beta_{2k}^{1/2k}$ diverges. In this case, according to Theorem 3, we have $\Phi_{\mathcal{X}}(\mathbf{t}) = \Phi_{\mathcal{Y}}(\mathbf{t})$ when \mathbf{t} samples around $\mathbf{0} \rightarrow \mathcal{X} =^d \mathcal{Y}$. Conversely, it is obvious that $\mathcal{X} =^d \mathcal{Y} \rightarrow \Phi_{\mathcal{X}}(\mathbf{t}) = \Phi_{\mathcal{Y}}(\mathbf{t})$ for all \mathbf{t} . Therefore, as for bounded \mathcal{X} and \mathcal{Y} , sampling around $\mathbf{0}$ is sufficient to ensure the symmetry, triangle, non-negativity (together with the uniqueness when the equality holds) properties of $\mathcal{C}_{\mathcal{T}}(\mathcal{X}, \mathcal{Y})$.

This completes the proof.

Proof of Lemma 3: We first show the boundedness of $\mathcal{C}_{\mathcal{T}}(\mathcal{X}, \mathcal{Y})$ by observing

$$\begin{aligned} 0 \leq \mathcal{C}_{\mathcal{T}}(\mathcal{X}, \mathcal{Y}) &= \int_{\mathbf{t}} |\Phi_{\mathcal{X}}(t) - \Phi_{\mathcal{Y}}(t)| dF_{\mathcal{T}}(\mathbf{t}) \\ &\leq \int_{\mathbf{t}} |\Phi_{\mathcal{X}}(t)| dF_{\mathcal{T}}(\mathbf{t}) + \int_{\mathbf{t}} |\Phi_{\mathcal{Y}}(t)| dF_{\mathcal{T}}(\mathbf{t}) \leq 1 + 1 = 2, \end{aligned} \quad (12)$$

where the second inequality is obtained via the Minkowski inequality and the third one by the fact that the maximal modulus of the CF is 1. It needs to be pointed out that this property is important and advantageous because in this way our cost is bounded automatically. Otherwise, we may need to bound $f \in \mathcal{F}$ to ensure an existence of the supremum of some IPMs (such as the dual form of the Wasserstein distance used in the W-GAN).

To prove the differentiable property, we first expand $c(\mathbf{t})$ in $\mathcal{C}_{\mathcal{T}}(\mathcal{X}, \mathcal{Y}) = \int_{\mathbf{t}} \sqrt{c(\mathbf{t})} dF_{\mathcal{T}}(\mathbf{t})$ as

$$c(\mathbf{t}) = (\operatorname{Re}\{\Phi_{\mathcal{X}}(\mathbf{t})\} - \operatorname{Re}\{\Phi_{\mathcal{Y}}(\mathbf{t})\})^2 - (\operatorname{Im}\{\Phi_{\mathcal{X}}(\mathbf{t})\} - \operatorname{Im}\{\Phi_{\mathcal{Y}}(\mathbf{t})\})^2, \quad (13)$$

where $\operatorname{Re}\{\Phi_{\mathcal{X}}(\mathbf{t})\} = \mathbb{E}_{\mathcal{X}}[\cos(\mathbf{t}^T \mathbf{x})]$ denotes the real part of the CF and $\operatorname{Im}\{\Phi_{\mathcal{X}}(\mathbf{t})\} = \mathbb{E}_{\mathcal{X}}[\sin(\mathbf{t}^T \mathbf{x})]$ for its imaginary part. Therefore, by regarding $c(\mathbf{t})$ as a mapping $\mathbb{R}^m \rightarrow \mathbb{R}$, it is differentiable almost everywhere³. Due to the fact that the composition of differentiable functions is also differentiable, we conclude that $\mathcal{C}_{\mathcal{T}}(f(\mathcal{X}), f(\mathcal{Y}))$ is differentiable and continuous almost everywhere when $f(\cdot)$ is differentiable (e.g., the neural net).

This completes the proof.

Proof of Lemma 4: Because $\mathbb{E}_{\mathcal{Z}}[\|\mathbf{z} - f(g(\mathbf{z}))\|_2^2] = 0$ and $\|\mathbf{z} - f(g(\mathbf{z}))\|_2^2 \geq 0$, we have $\mathbf{z} = f(g(\mathbf{z}))$ for any \mathbf{z} and $g(\mathbf{z})$ under the supports of \mathcal{Z} and \mathcal{Y} , respectively. We can obtain $g(\mathbf{z}) = g(f(g(\mathbf{z})))$ under the supports of \mathcal{Z} and \mathcal{Y} as well; given that $\bar{\mathbf{y}} = g(\mathbf{z})$ by the definition, this results in $\bar{\mathbf{y}} = g(f(\bar{\mathbf{y}}))$. Then, we have $\mathbb{E}_{\mathcal{Y}}[\|\bar{\mathbf{y}} - g(f(\bar{\mathbf{y}}))\|_2^2] = 0$. Therefore, the function $g(\cdot)$ is a unique inverse of the function $f(\cdot)$, and vice versa, which also indicates that the two functions are bijective.

The bijection of the function $f(\cdot)$ possesses many desirable properties between the domains of $\bar{\mathcal{Y}}$ and \mathcal{Z} , thus ensuring the equivalences between their CFs. Specifically, without loss of generality, we assume $\mathcal{C}_{\mathcal{T}}(\bar{\mathcal{X}}, \bar{\mathcal{Y}}) = 0$, which means

$$\int_{\bar{\mathbf{x}}} e^{j\bar{\mathbf{t}}^T \bar{\mathbf{x}}} dF_{\bar{\mathcal{X}}}(\bar{\mathbf{x}}) = \int_{\bar{\mathbf{y}}} e^{j\bar{\mathbf{t}}^T \bar{\mathbf{y}}} dF_{\bar{\mathcal{Y}}}(\bar{\mathbf{y}}), \quad \text{for all } \bar{\mathbf{t}}. \quad (14)$$

Then, given the bijection $f(\cdot)$ by $\mathcal{X} = f(\bar{\mathcal{X}})$ and $\mathcal{Y} = f(\bar{\mathcal{Y}})$, we can obtain that $\mathbf{x} = f(\bar{\mathbf{x}}) = f(\bar{\mathbf{y}}) = \mathbf{y} \Leftrightarrow \bar{\mathbf{x}} = \bar{\mathbf{y}}$, for any realisations \mathbf{x} and \mathbf{y} from \mathcal{X} and \mathcal{Y} . We then have the following equivalence between the CFs of $\mathcal{X} = f(\bar{\mathcal{X}})$ and $\mathcal{Y} = f(\bar{\mathcal{Y}})$,

$$\begin{aligned} \int_{\bar{\mathbf{x}}} e^{j\bar{\mathbf{t}}^T \bar{\mathbf{x}}} dF_{\bar{\mathcal{X}}}(\bar{\mathbf{x}}) &= \int_{\bar{\mathbf{y}}} e^{j\bar{\mathbf{t}}^T \bar{\mathbf{y}}} dF_{\bar{\mathcal{Y}}}(\bar{\mathbf{y}}), \quad \text{for all } \bar{\mathbf{t}} \\ \Leftrightarrow \int_{\bar{\mathbf{x}}} e^{j\mathbf{t}^T f(\bar{\mathbf{x}})} dF_{\bar{\mathcal{X}}}(\bar{\mathbf{x}}) &= \int_{\bar{\mathbf{y}}} e^{j\mathbf{t}^T f(\bar{\mathbf{y}})} dF_{\bar{\mathcal{Y}}}(\bar{\mathbf{y}}), \quad \text{for all } \mathbf{t} \\ \Leftrightarrow \int_{\mathbf{x}} e^{j\mathbf{t}^T \mathbf{x}} dF_{\mathcal{X}}(\mathbf{x}) &= \int_{\mathbf{y}} e^{j\mathbf{t}^T \mathbf{y}} dF_{\mathcal{Y}}(\mathbf{y}), \quad \text{for all } \mathbf{t}. \end{aligned} \quad (15)$$

Therefore, we have $\mathcal{C}_{\mathcal{T}}(f(\bar{\mathcal{X}}), f(\bar{\mathcal{Y}})) = 0$. Furthermore, we also have $f(\bar{\mathcal{Y}}) \stackrel{d}{=} \mathcal{Z}$ due to $\mathbb{E}_{\mathcal{Z}}[\|\mathbf{z} - f(g(\mathbf{z}))\|_2^2] = 0$. Therefore, we have the following equivalences: $\mathcal{C}_{\mathcal{T}}(\bar{\mathcal{X}}, \bar{\mathcal{Y}}) = 0 \Leftrightarrow \mathcal{C}_{\mathcal{T}}(f(\bar{\mathcal{X}}), f(\bar{\mathcal{Y}})) = 0 \Leftrightarrow \mathcal{C}_{\mathcal{T}}(f(\bar{\mathcal{Y}}), \mathcal{Z}) = 0$ and $\mathcal{C}_{\mathcal{T}}(f(\bar{\mathcal{X}}), \mathcal{Z}) = 0$.

This completes the proof.

C Related Works

IPM-GANs: Instead of the naive weight clipping in the W-GAN [5], the gradient penalty W-GAN (W-GAN-GP) was proposed to mitigate the heavily constrained *critic* by penalising the gradient norm [8], followed by a further elegant treatment of restricting the largest singular value of the net weights [9]. It has been understood that although the *critic* cannot search within all satisfied Lipschitz functions [6, 7], the *critic* still performs as a way of transforming high dimensional but insufficiently supported data distributions into low dimensional yet broadly

³Please note that $c(\mathbf{t})$ is not necessarily complex differentiable because it does not satisfy the Cauchy-Riemann equations. It is the fact that any *nonconstant purely real-valued functions* are not complex differentiable because their Cauchy-Riemann equations cannot be satisfied. However, in our case of regarding it as mappings in the real domain, it is differentiable. Please refer to [46, 47] for more detail in the $\mathbb{C}\mathbb{R}$ calculus.

supported (simple) distributions in the embedded domain [14]. Comparing the embedded statistics, however, is much easier. For example, Cramer GAN compared the mean with an advanced \mathcal{F} from the Cramer distance to correct the biased gradient [48], whilst McGAN [11] explicitly compared the mean and the covariance in the embedded domain. Fisher GAN employed a scale-free Mahalanobis distance and thus data dependent \mathcal{F} [10], which is basically the Fisher-Rao distance in the embedded domain between two Gaussian distributions with the same covariance. The recent Sphere GAN further compared higher-order moments up to a specified order, and avoided the Lipschitz condition by projecting onto a spherical surface [12]. Moreover, in a non-parametric way, BE-GAN directly employed an auto-encoder as the *critic*, whereby the auto-encoder loss was compared through embedded distributions [49]. The sliced Wasserstein distance has also been utilised in measuring the discrepancy in the embedded domain [50]. Another non-parametric metric was achieved by the kernel trick of the MMD-GAN [13, 14], which assumed \mathcal{F} as the reproducing kernel Hilbert space. However, as one of the most powerful ways of representing a distribution, the CF, is still to be fully explored. More importantly, our RCF-GAN fully compares the embedded distributions and also generalises the MMD-GAN by flexible sampling priors.

Auto-encoders in an adversarial way: To address the smoothing artefact of the variational auto-encoder [40], several works aim to incorporate the adversarial style in (variational) auto-encoders, in the hope of gaining clear images whilst maintaining the ability of reconstruction. These mostly consist of at least three modules, an encoder, a decoder, and an adversarial modules [21–26]. To the best of our knowledge, the one exception, called the adversarial generator encoder (AGE) [20], only incorporated two modules in adversarially training an auto-encoder under a max-min problem. The AGE still assumes the Gaussianity in the embedded distributions and only compares the mean and the diagonal covariance matrix; this is basically insufficient in identifying two distributions, in which the pixel domain loss was utilised supplementally. However, the initiative of this paper is fundamentally different from the AGE, and the auto-encoder in our RCF-GAN aims to achieve the theoretical guarantee of a bijection, with different losses proposed for the *critic* and the generator. Furthermore, other than the first- and second-order moments, our work fully compares the discrepancies in the embedded domain via CFs. Benefiting from the powerful non-parametric metric via the CFs, our RCF-GAN only adversarially learns distributions in the embedded domain, that is, on a semantically meaningful manifold, without the need of any operation on the data domain.